ADVANCED SENSOR RESEARCH Open Access
www.advsensorres.com

Multiplexed Piezoelectric Electronic Skin with Haptic Feedback for Upper Limb Prosthesis

*Muhammad Awais, Easa AliAbbasi, Abdulkadir Yasin Atik, Mohammad Javad Bathaei, Mohsin Ali, Ritu Das, Cagdas Dag, Azmat Ullah, Rahul Singh, Kemal Sitki Turker, Cagatay Basdogan, and Levent Beker**

Upper limb amputation severely impairs tactile perception, limiting daily activities. Developing a near-natural replacement with prosthetic devices requires improving user sensory experiences during object interactions. The ideal upper limb prosthesis should provide real-time sensory feedback, mirroring natural experiences. Current prostheses struggle with providing adequate tactile feedback due to sensory limitations. Inspired by the sensory properties of skin, we present a micro-fabricated, multiplexed electronic skin (e-skin) with actuators for sensory feedback in upper limb amputation. The piezoelectric-capacitive sensor array detects static pressure, temperature, vibration, and texture, with integrated actuators stimulating the skin to provide real-time feedback. The sensors integrate with actuators via readout electronics, making the system standalone and easy to use. The flexible, compact sensor array design (two pixels within a 1 cm^2 footprint) detects a wide range of pressure (0.5–10 kPa), temperature (22–60 °C), vibration (35–100 Hz), and texture (2.5–45 Hz), suitable for daily use. The e-skin, attached to a prosthetic finger, is tested for feasibility on human volunteers with wrist-mounted actuators. Statistics are used to quantitatively assess system performance. The integration of multiplexed sensors and actuators enhances tactile feedback, improving the quality of life for people with upper limb amputations.

1. Introduction

An aging population, increased accidents, health-related amputations, an increase in diabetic cases, and complications from vascular diseases all contribute to the rising global demand for limb prostheses.[1] While prosthetic limbs have evolved to restore motor functions, replicating the intricate sense of touch found in human skin remains a significant challenge. It is expected that by 2050, ≈3.6 million people in the United States will use prosthetic limbs as assistive devices.[2] Human skin receptors detect tactile stimuli such as pressure, temperature, vibration, and texture.[3] As a result, a continuous sensing mechanism is required to closely mimic human skin's sensitivity and responsiveness to different stimuli. With ongoing advancements in the e-skin technology, the restoration of human tactile sensing in prosthetic hands becomes possible. E-skin has the potential to be used in a variety of applications, including haptic feedback,[4–8]

M. Awais, M. J. Bathaei, M. Ali, A. Ullah, C. Basdogan, L. Beker
Department of Biomedical Sciences and Engineering
Koç University
Rumelifeneri Yolu, Sarıyer, Istanbul 34450, Turkey
E-mail: lbeker@ku.edu.tr

E. AliAbbasi, C. Basdogan
Department of Computational Sciences and Engineering
Koç University
Rumelifeneri Yolu, Sarıyer, Istanbul 34450, Turkey

A. Y. Atik, R. Das, R. Singh, C. Basdogan, L. Beker
Department of Mechanical Engineering
Koç University
Rumelifeneri Yolu, Sarıyer, Istanbul 34450, Turkey

C. Dag, L. Beker
Nanofabrication and Nanocharacterization Centre for Scientific and Technological Advanced Research
Koç University
Rumelifeneri Yolu, Sarıyer, Istanbul 34450, Turkey

K. S. Turker
Faculty of Dentistry
Istanbul Gelisim University
Cihangir, Şehit Jandarma Komando, J. Kom. Er Hakan Öner Sk. No:1, Avcılar, İstanbul 34310, Turkey

The ORCID identification number(s) for the author(s) of this article can be found under https://doi.org/10.1002/adsr.202400100

DOI: 10.1002/adsr.202400100

prosthetics,[9–14] intelligent robotics,[15–20] human-machine interfaces, and more.[21,22] However, an ideal e-skin system must be multifunctional in order to detect multiple types of stimuli[23–26] while also instilling a sense of ownership or embodiment of the prosthetic limb.[27]

E-skin is typically made of flexible and stretchable materials that can detect physical parameters similar to the human sense of touch. While the implementation of sensations such as pressure, temperature,[7] and pressure,[12] vibration, and texture[28,29] has made gradual progress, the human tactile system's full multifunctional capacity is still underestimated. As a result, multifunctional e-skins made of stretchable matrix networks have been proposed for pressure, temperature, and material sensing.[30–33] These e-skins use a variety of phenomena, including piezoelectricity, piezo resistivity, and triboelectricity, to allow for material discrimination and texture recognition.[34–37] The combination of capacitive and piezoelectric effects in e-skins allowed the detection of position, dynamic force, proximity, and humidity while maintaining a much simpler structure.[38] Furthermore, integrating diverse units through a well-thought-out combination of functional and structural design resulted in the development of an e-skin with multifunctional capabilities for pressure, wind flow, and thermosensation-based material recognition.[26] On the other hand, e-skin has the potential to allow robots to interact with the world in a more intuitive, safe, and efficient manner. As a result, incorporating multifunctional sensing e-skin into robots that can sense contact force, position, temperature, and proximity improved overall human-robot interaction.[39] However, the integration of these skins onto prosthetic or robotic hands requires specific designs, a challenge addressed by the fabrication of 3D-shaped e-skins.[40] Even though individual sensors have been developed for e-skin applications, it is critical to provide a solution or design that allows for a simple fabrication process, multiplexed sensing capabilities, and the possibility of miniaturization to increase pixel density. Furthermore, limited research has been conducted on combining multiplexed sensors with actuators to achieve comprehensive haptic feedback. Integrating these sensors and actuators directly through the readout electronics makes the system standalone and significantly reduces the bulkiness of the e-skin. This innovative integration not only enhances functionality but also streamlines the overall design for more practical and efficient use.

To address the identified issues, we propose a novel microfabricated e-skin featuring miniaturized arrays of sensors capable of detecting static pressure, temperature, vibration, and texture. By utilizing capacitive and piezoelectric sensing through single piezoelectric layer microfabrication, as well as in-plane and double plate electrode designs, we ensure that these sensors are designed to integrate seamlessly with readout electronics. The designed electronic circuit is a miniaturized (2.5 cm × 2.5 cm) double-sided circuitry that contains a microcontroller and other peripheral devices for signal processing. This integration makes the system standalone, eliminating the need for external processing units. Our e-skin is specifically designed for upper limb amputations, with a comprehensive test protocol developed to assess its performance in various daily activities. Additionally, a set of four actuators at the wrist provides real-time sensation transmission. Through experiments, we demonstrate our e-skin system's broad sensing range, enabling simultaneous detection of multiple stimuli and feedback via actuators. Our e-skin system has been successfully validated in human trials, showcasing its potential for diverse applications, including prosthetics, wearable health monitoring, and human-robot interaction.

2. Results and Discussion

2.1. The Working Mechanism

The multiplexed, piezoelectric-capacitive-based e-skin system developed in this work transmits the static pressure, temperature, vibration, and texture sensations picked up by the sensors to a group of actuators to provide real-time feedback. **Figure 1A** illustrates the concept of the e-skin system implemented on a hand prosthesis for the tactile information collection, transmission, and generation of artificial sensation in the human body. Once the tactile signals are received by the sensors, the corresponding actuators are triggered to replicate the production of the sensations to the skin. The exploded view consists of different layers of flexible materials that are used for the fabrication of the single-pixel array of the sensor (right panel of Figure 1A).

The temperature and static pressure sensors produce a capacitance variation in response to external temperature and static pressure stimuli, respectively (right panel of Figure 1B). Likewise, the vibration and texture sensor generates a potential difference due to the piezoelectric effect when subjected to external vibration and texture stimuli, respectively (left panel of Figure 1B). The e-skin system can be mounted on the amputated arm with a sensor array attached to the finger of the prosthetic hand to collect data when the finger is interacting with external objects, while the actuators are placed on the wrist of the human hand for the feedback mechanism (Figure 1C; Figure S1, Supporting Information). The standalone electronic circuit serving as the core part of the e-skin system consists of a microcontroller unit together with other electronic components to receive the data from the sensors, process the data, and send it to the actuators.

Figure 1D shows a fabricated single-pixel array of sensors having a total area of 1 cm^2 and contains four types of sensors. A microfabricated pyramid structure was placed on top of the pressure sensor which enhances the sensitivity of the sensor by maximizing the effective deformation of dielectric material (Figures S2 and S3, Supporting Information). With the use of a pyramid structure, the applied force leads to a more pronounced change in the capacitance between the interdigitated electrodes, making the sensor more responsive to subtle pressure changes. We also calculated the bending stiffness of our device which has the value of 4.94 pN m^{-1} (Text S1, Supporting Information). Similarly, a ridge was attached to one side of the texture sensor, which applies tension on the sensor when subjected to the rough surface (Figure S4, Supporting Information). To demonstrate the miniaturization potential of the e-skin system using the microfabrication approach, a 2 × 2 array of sensors with the dimensions of (0.32 cm^2) was fabricated through simple spin coating and thermal evaporation processes (Figure 1E). The 2 × 2 array of sensors is as thin as 115 μm after the protection layer on top and bottom. Our fabrication design has the capability that the sensors array can be further miniaturized to have more sensors in a small area. We have shown that the same area (0.32 cm^2) can also be utilized

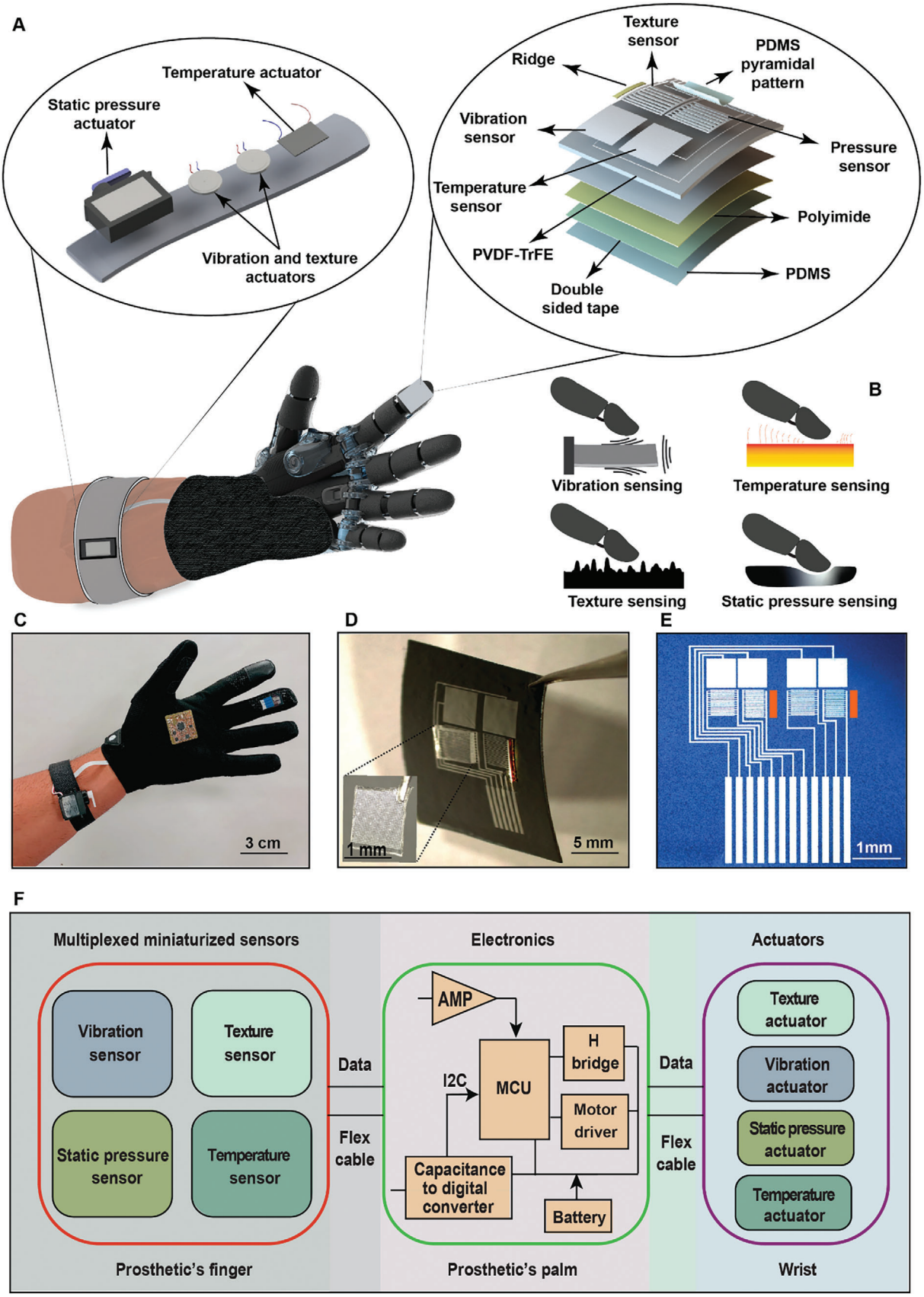

to fabricate a 3 × 3 array of sensors (Figures S5–S29, Supporting Information).

Our e-skin system can be represented in three main subsystems: i) a multiplexed piezoelectric sensor to gather haptic information during contact with an object; ii) a miniaturized printed circuit board (PCB) that reads the data from the sensor and sends the data to the actuators; iii) a velcro band that contains actuators to stimulate the healthy area of the skin (Figure 1F). The sensors and actuators used in this setup have a fast response time between the sensation by the sensors on the residual limb and the actuation on the human skin. The velcro attached to the upper limb provides a soft interface of the actuators to the skin which makes the system easy to use.

2.2. Characterization of the Pressure and Temperature Sensors and Actuators

The static pressure sensor specifically employs an interdigitated multi-finger periodic structure. This sensor possesses crucial characteristics such as rapid response, excellent linearity, long-term stability, and a wide operating range. The pyramidal shape made of polydimethylsiloxane was placed on the sensor and the change in dielectric constant of the sensor stemming from the geometrical shape change in the pyramidal structure due to the applied pressure. The applied external pressure leads to a change in output capacitance (**Figure** 2A). The fabricated pressure sensor is characterized as an interdigitated capacitance sensor, which calculates the capacitance using Equation (1).

$$C = (n-1) * \frac{\varepsilon_r * \varepsilon_0 * W * t}{d} \tag{1}$$

In this equation, C represents the measured capacitance value. ε_0 and ε_r correspond to the permittivity of free space and the dielectric layer, respectively. W represents the overlapped length of electrodes,d denotes the distance between the two electrodes, t indicates the thickness of the conductive electrode, and n signifies the number of interdigital electrodes within the structure. We selected PVDF-TrFE (polyvinylidene fluoride-trifluoro ethylene) as a dielectric layer that possesses a relatively high dielectric constant ($\epsilon_r = 10.5$). This property enhances the capacitance change between the interdigitated electrodes, making the sensor more sensitive to pressure variations. The choice of PVDF for all sensors may not be optimal regarding sensitivity, measurement range, and response time, but it was adequate for the acceptable range of daily activities in our application. The developed temperature sensor utilizes a parallel plate capacitive configuration. As the external temperature changes, the relative permittivity of the dielectric layer in the sensor increases, resulting in a corresponding increase in capacitance (Figure 2B). The capacitance of the parallel plate temperature sensor can be demonstrated according to Equation (2).

$$C = \varepsilon_r \varepsilon_0 A/d \tag{2}$$

where, ε_r is the permittivity of the dielectric, ε_0 is the permittivity of the free space, A is the area of the plates, and d is the distance between the two plates (i.e., the thickness of the dielectric). Figure 2C shows the top view SEM image of the pressure sensor (Figure S28, Supporting Information), while Figure 2D displays the image of the temperature sensor.

To record the change in capacitance resulting from the applied pressure on the sensor, an impedance analyzer (MFIA, Zurich Instruments) synchronized with a force gauge was employed. The measured capacitance is a linear function of pressure and remains unchanged when the applied pressure (10 kPa) remains constant. To record the change in capacitance resulting from the applied pressure on the sensor, an impedance analyzer (MFIA, Zurich Instruments) synchronized with a force gauge was employed. The measured capacitance shows an increasing trend with the increase in the applied pressure (Figure 2E). Under cyclic loading and unloading, the capacitance of the interdigitated capacitive sensor varies as expected in response to the applied pressure. When the force was applied, the capacitance changed accordingly, and upon removal of the force (when it becomes zero), the capacitance returned to its initial value (Figure 2F). The extracted calibration curve is linear for different applied external pressures, ranging from 1–10 kPa (Figure 2G). To show the standalone capability of the e-skin system, we conducted different experiments in which the sensor was connected to the miniaturized electronic circuitry using a flexible cable. A loading/unloading test was conducted, during which the change in capacitance was recorded utilizing the capacitance to digital converter (CDC) integrated circuit (IC) (FDC1004, Texas Instruments Inc.) (Figure S6, Supporting Information). Figure 2H illustrates the anticipated response of the pressure sensor to cyclic loading and unloading, demonstrating that the capacitance of the sensor promptly returns to its initial value without any noticeable delay.

Human skin sensitivity ranges from 0 to 10 kPa, perceiving light touch.[41,42] To simulate this, a servo motor serves as an actuator, attached via a velcro strip on the wrist. Controlled rotation of the motor arm replicates mild tactile sensations (Movie S1, Supporting Information). This mechanism mimics human skin perception. Figure 2I displays servo motor-induced pressure measured by a force transducer (Nano17, ATI Inc.). The pressure of the motor on the skin correlates with external pressure on the sensor, altering capacitance. The motor's arm, as it rotates toward the skin, applies greater pressure. By adjusting the sensor's external pressure, control over skin pressure is achieved. The arm's rotation level corresponds to the pressure applied, effectively regulating skin pressure. This allows the replication of gentle tactile sensations perceived by human skin.

Figure 1. Schematic illustration and overview of a multifunctional sensory feedback e-skin for the upper limb amputation. A) Schematic illustration of our e-skin system. B) Exploded view of the 2 pixels of miniaturized sensors containing different layers of the sensors. C) Picture of the e-skin setup worn by a person with the glove to mimic the prosthetic hand and the velcro on the wrist. D) Picture of the e-skin system attached to a glove. E) Optical image of a single pixel array of e-skin sensors highlighting its miniaturized and flexible form factor. F) Functional block diagram showing the e-skin system in three parts: Multiplexed, piezoelectric-capacitive based array of sensors, a miniaturized electronic circuitry with flexible connection, and actuators for each corresponding sensor.

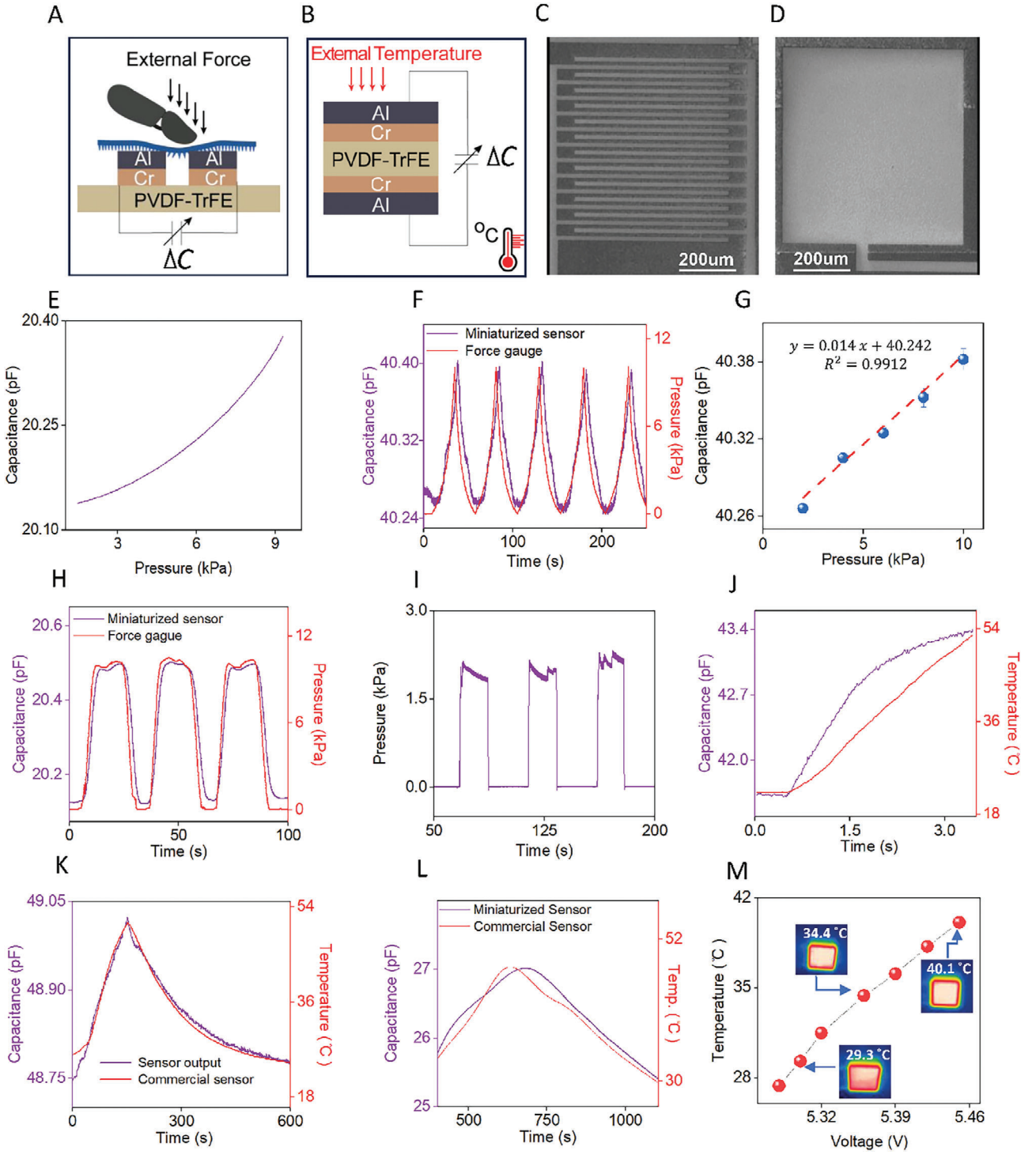

Figure 2. Performance characteristics of the pressure and temperature sensor and their corresponding actuators. A) Working mechanism of the miniaturized pressure sensor. B) working principle of the temperature sensor. C) SEM (Scanning electron microscopy) image of the miniaturized pressure sensor. D) SEM image of the soft temperature sensor. E) Increasing response of the change in capacitance with the change in applied pressure. (ΔC) with respect to the applied pressure. F) Change in capacitance of the sensor under four cycles of loading/unloading compared to the measurements using a force gauge. G) Change in capacitance of the sensor under four cycles of loading/unloading compared to the measurements using a force gauge. H) Change in capacitance of the sensor connected to the electronics under three loading/unloading cycles compared to the measurements using a force gauge. I) Response of the pressure actuator to produce a soft touch in response to the applied pressure of the sensor. J) Linear response of the temperature sensor to the applied external temperature. K) Variation of capacitance with the applied external temperature to the sensor connected to the impedance analyzer. L) Response of the miniaturized temperature sensor to the external temperature in comparison with the commercial sensor connected to the electronics. M) The output of the temperature actuator to the increase in applied voltage.

To demonstrate the performance of the temperature sensor, it was connected to the impedance analyzer and the external temperature was applied by using a heat gun. The change in applied temperature leads to the change in the capacitance of the sensor, which can be demonstrated in the form of the linear relationship between the change in capacitance and the applied external temperature (Figure 2J). The output of the sensor was compared with the commercial temperature sensor (MPL3115A2, NXP USA Inc.) by applying external temperature to both the fabricated sensor and commercial sensor simultaneously. Figure 2K demonstrates the capacitance response of the fabricated temperature sensor along with a commercial temperature sensor to external temperature variations. The capacitance increases as the external temperature increases and then the sensor returns to its initial capacitance when the temperature starts to decrease. The output of the sensor shows a good correlation with the commercial sensor. The sensor was then connected to the standalone miniaturized electronics to record the change in capacitance by using a CDC IC. The fractional change of the analog-to-digital converter (ADC) values acquired from the miniaturized PCB is presented in response to different temperatures (Figure 2L). The temperature change, ranging from ≈30 to 50 °C, was correlated with the corresponding change in capacitance when the temperature was applied to the miniaturized sensor. The data obtained from the miniaturized sensor shows good agreement with the readings from the commercial sensor.

To generate a temperature sensation on the human skin, the temperature actuator was placed on the wrist of the human hand. A Peltier module was utilized as a temperature actuator which is capable of generating a temperature difference between its two sides when a voltage difference is applied. When the capacitance of the sensor deviates from its initial value, a logic high signal is sent to a digital pin on the microcontroller. This signal triggers the actuator, thereby activating the Peltier effect and resulting in the applied temperature sensation on the skin. Given that the warm thermoreceptors of the human skin are typically stimulated in the temperature range of 25–40 °C,[43] it is crucial for the actuators to respond swiftly within this range. Figure 2M represents the characteristic curve of the actuator's temperature whose temperature could be easily increased to a high temperature with low voltage. The relationship between the voltage and the final maintained temperature is plotted. As the PWM (pulse width modulation) signal stimulation is given to the actuator, the voltage output to the actuator is controlled by the H-bridge.

2.3. Characterization of Vibration Sensor and Actuator

Our skin is more sensitive to mechanical vibrations within the frequency range of 40–400 Hz.[44,45] To replicate the vibration-sensing ability of human skin, we designed a piezoelectric-based vibration sensor. This sensor detects external mechanical vibrations of varying frequencies and generates an output voltage in response. The sensor follows a parallel plate configuration, utilizing PVDF-TrFE as the dielectric layer. Specific design details and the fabrication process are elaborated in the Experimental Section to provide further insights into the sensor structure and construction. PVDF is a piezoelectric plastic material with a unique property: when subjected to mechanical deformation, it generates equal and opposite charges on both sides of the film. In the case of our piezoelectric-based vibration sensor, external vibrations cause the PVDF film to align its dipoles in a specific direction, from the top layer to the bottom. This alignment results in a potential difference in the external circuit (**Figure 3A**). The amplitude of the voltage produced in the external circuit is directly proportional to the amplitude of the applied vibration. Hence, higher-amplitude vibrations induce higher-voltage outputs from the sensor. This behavior enables the sensor to accurately capture and quantify the magnitude of external vibrations based on the resulting voltage signals. Figure 3B presents the SEM image of the top view of the vibration sensor.

To induce vibrations, the sensor was subjected to a vibrating beam with a vibration motor attached underneath it (Figure S7, Supporting Information). The output of the piezoelectric vibration sensor was connected to an oscilloscope to record the data in the form of an output voltage signal. The voltage signal recorded with an oscilloscope with a sampling frequency of 100 kS s^{-1}, is presented in Figure 3C for 10 s. To eliminate any 50 Hz environmental noise, the signal was passed through a notch filter with a notch frequency of 50 Hz. This filtering process helps to enhance the clarity of the vibration signal. To validate the capability of the vibration sensor to detect a wide range of frequencies, high-frequency vibrations were applied to the sensor. Figure 3D,E depict the resulting voltage signals generated by increasing the external vibration, respectively. To confirm the frequency of the vibration sensor, a Fast Fourier Transform (FFT) analysis was performed using MATLAB. The resulting FFT plot in Figure 3F reveals the dominant frequency in the output signal to be 60 Hz, validating the vibration sensor-generated frequency. To confirm the dominant frequency present in high-frequency signals, the FFT response was calculated. Figure 3G displays the FFT signal of waveform Figure 3D, showing a dominant frequency of 80 Hz. Similarly, for the waveform obtained in Figure 3E, FFT analysis resulted in a dominant frequency peak at 100 Hz, as illustrated in Figure 3H. These analyses demonstrate the accurate capturing and differentiation of various frequencies of the vibration sensor within its operating range, including lower and higher frequencies.

We conducted a performance comparison with a commercial accelerometer to verify the dominant frequency produced by our vibration sensor. Both the vibration sensor and the accelerometer were placed adjacent to each other on the vibrating beam and connected to an oscilloscope (Text S1, Supporting Information). The output of the accelerometer was recorded in the form of a voltage waveform recorded at a sampling frequency of 100 kS s^{-1} (Figure S8, Supporting Information). To confirm the dominant frequency, FFT analysis was performed on both waveforms. The FFT analysis revealed a dominant frequency of 80 Hz for both the vibration sensor and the accelerometer, indicating consistency between the two measurements (Figure S9, Supporting Information). Furthermore, to confirm the dominant frequency of 100 Hz, the output of the accelerometer was also obtained (Figure S10, Supporting Information). The FFT analysis was performed on the voltage waveform, and the 100 Hz frequency was confirmed (Figure S11, Supporting Information). The comparison of the fabricated sensor with the commercial sensor confirms the functionality of the sensor.

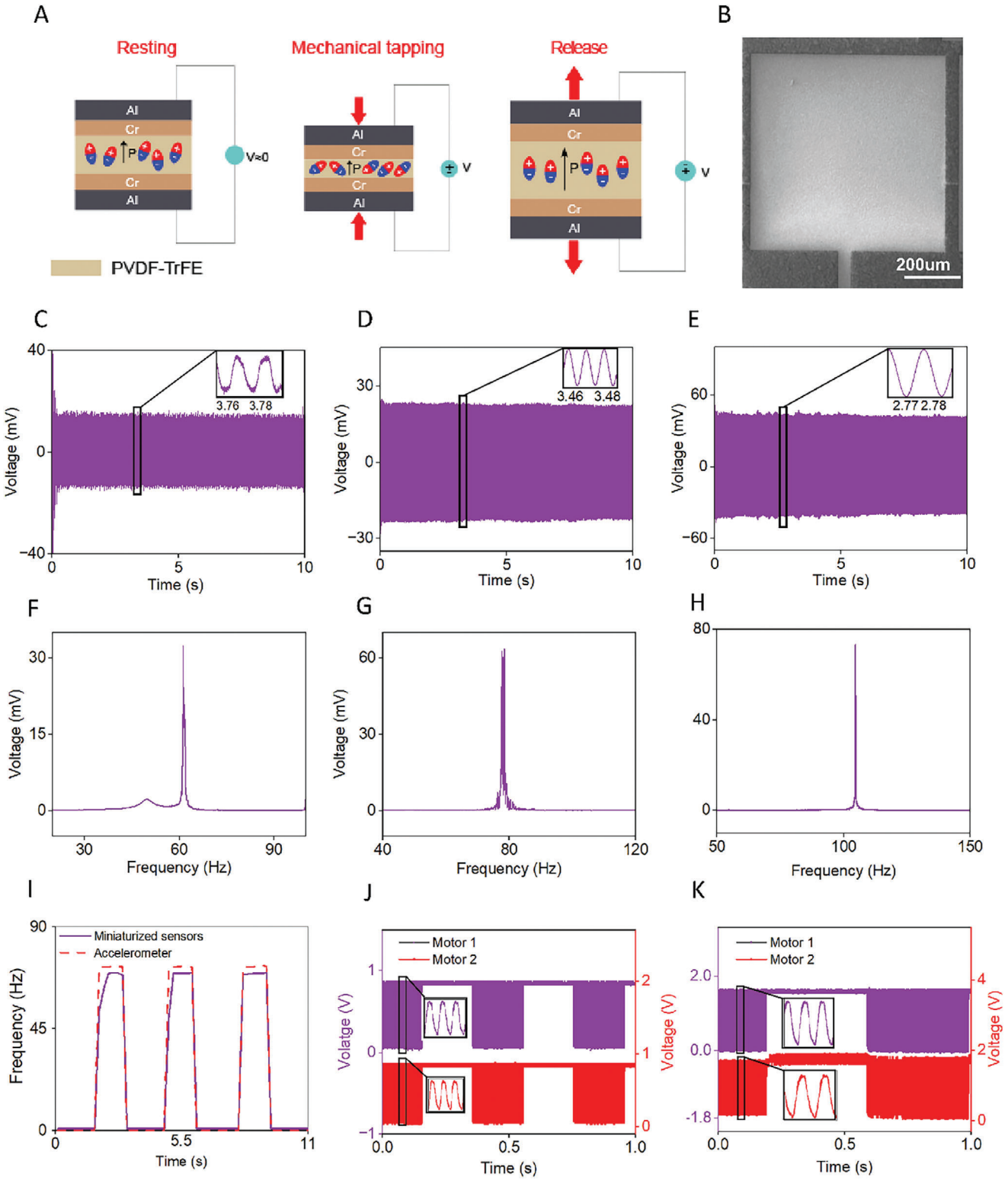

Figure 3. Characterization of piezoelectric-based vibration sensor and actuator. A) Working mechanism of the piezoelectric-based vibration sensor. B) SEM image of the vibration sensor. C) The voltage waveform of the output signal of 60 Hz vibration. D) Dominant peak signal of the 35 Hz vibration signal. E) The voltage waveform of the output signal of 80 Hz vibration. F) Dominant peak signal of the 45 Hz vibration signal. G) The voltage waveform of the output signal of 100 Hz vibration. H) Dominant peak signal of the 60 Hz vibration signal. I) Vibration sensor connected to the electronics circuit which calculates the dominant frequency of the externally applied vibration. J,K) PWM output of two coin-cell motors vibrating simultaneously with frequencies of 100 and 80 Hz, respectively.

To evaluate the performance of the stand-alone system, we connected the vibration sensor to the miniaturized double-sided PCBspecifically designed for our e-skin system. We conducted a real-time FFT analysis of the input signal received by the microcontroller from the sensor. Figure 3I illustrates the output signal produced by the microcontroller, which involves identifying the dominant frequency using FFT analysis. When there was no external vibration, the output of the FFT produced a zero value of dominant frequency. Similarly, when there was an external vibration applied to the system, a non-zero value of dominant frequency was obtained. This dominant frequency was further validated by comparing it with the output FFT signal obtained from the accelerometer. By comparing the FFT signals from both the sensor output and the accelerometer, we can confirm the accuracy and consistency of the dominant frequency determined by our standalone system. This analysis ensures that the system effectively captures and processes the vibration data, providing reliable information about the dominant frequency.

To create the sensation of vibration on the skin, we incorporated coin cell vibration motors as vibration actuators.[46] These eccentric rotating mass (ERM) motors (VC1026B002F, Vybronics Inc.) were specifically chosen to vibrate at the same dominant frequencies produced by the vibration sensor. To synchronize the actuation with the sensor output, we utilized a motor driver (DRV2605, Texas Instruments Inc.). The motor driver generated a PWM signal that was mapped with the dominant frequency obtained from the real-time FFT analysis conducted in the microcontroller. This mapped PWM signal was then used to drive the vibration motors, ensuring that they vibrated at the desired frequency. For vibration actuation, both motors operated simultaneously with the same PWM signal. Figure 3J,K demonstrates the operation of the two motors vibrating at 100 and 80 Hz, respectively, with synchronized PWM. This synchronized vibration actuation provides a realistic and coordinated vibration sensation to the user's skin.

2.4. Characterization of Texture Sensor and Actuator

There are two types of textures that human skin can sense; coarse textures, which are perceived by slow adapting mechanoreceptors and have a feature size of >100 μm, and fine textures, which are perceived by rapidly adapting (RA) mechanoreceptors and have a feature size of <100 μm. Fine textures are detected by fast adaptive receptors which are sensitive to the vibration generated by the relative motion between the skin and the object when sliding the finger over its surface.[47] Because of different depths and patterns, each texture produces unique data when moving on the surface of a sensor.

In our design, we have incorporated an interdigitated piezoelectric sensor as the texture sensor. Our texture sensor is designed for detecting low-frequency rough textures. This sensor is capable of generating a voltage output when it comes into contact with an external textured surface, allowing us to capture and analyze the tactile information of the surface. To enhance the detection of surface textures, a ridge made from Kapton tape was attached to the edge of the sensor surface (Figure S12, Supporting Information). This ridge has specific dimensions, with a width of 0.3 mm and a height of 1 mm, providing a defined contact area for the sensor to interact with the textured surface. When the sensor slides on a rough surface, the ridge produces tension on the sensor, and the potential difference is generated between the interdigitated electrodes (**Figure** 4A). By analyzing the voltage output from the interdigitated piezoelectric sensor, our system can interpret the texture frequency information and provide haptic feedback to the users which enables them to perceive and distinguish different surface textures using a prosthetic hand. Figure 4B shows the top view of the SEM photo of the piezoelectric-based texture sensor with a ridge attached to its side.

In the texture sensor experiment, the rough surface was placed at a moving stage (LTS150, Thorlabs Inc.) containing a force sensor (Mini40-SI-80-4, ATI Inc.) with a controlled speed, and the sensor was placed on a fixed point to be in contact with the surface (Text S2 and Figure S13, Supporting Information). The voltage waveform was obtained by reading the output through an oscilloscope with a sampling frequency of 100 kS s^{-1}. The frequency obtained from the roughness of the surface depends on the spatial period of the texture and the speed with which the sensor is moving on a surface. The frequency can be determined from the following equation:

$$f = \frac{v}{\lambda} \tag{3}$$

where, f is the characteristic frequency, v is the sliding speed, and λ is the period width (grating size) of the texture. The output signal produced by the texture sensor can be observed as a voltage spike when the sensor was moving on a rough surface, and the characteristic frequency (2.5 Hz) was equivalent to the theoretical value of the calculated frequency (Figure 4C). With a fixed rate of 10 mm s^{-1}, a frequency of 2.5 Hz was obtained by making the spatial period 4 mm. The dominant frequency was calculated by taking the FFT in MATLAB with the notch filter of 50 Hz to remove the noise from the signal (Figure 4E). Similarly, the voltage waveform obtained by increasing the moving speed to 20 mm s^{-1} while keeping the roughness of the surface with a spatial period of 4 mm (Figure 4D). The dominant frequency was calculated by taking the FFT of the signal which confirms the frequency of 5 Hz (Figure 4F). The fabricated sensor can even detect textures having lower spatial periods. For example, we slide the sensor on a surface with periodic gratings at two different speeds (10 and 20 mm s^{-1}) and detect the spatial frequencies of 16 Hz (Figure S14, Supporting Information) and 18 Hz (Figure S15, Supporting Information).

The miniaturized array of sensors was then connected to the electronics by using a flexible cable connection to get the data from the sensor (Text S3, Supporting Information). The real-time FFT was performed at 400 Hz in the microcontroller to detect the dominant frequency of the sensor. Figure 4G illustrates the two frequencies of 20 and 30 Hz detected by moving the sensor on texture surfaces (the texture surfaces are shown in the top left corner of the figure) having the gratings with spatial periods of 1 and 0.66 mm, respectively, with a constant speed of 20 mm s^{-1} (Figure S16, Supporting Information). To produce the sensation of texture on the healthy part of the human body, we used two coin-cell ERM vibration motors. The motors were given a PWM signal with a certain delay between the actuation time, as shown in Figure 4H. The delay between the actuation time of the two

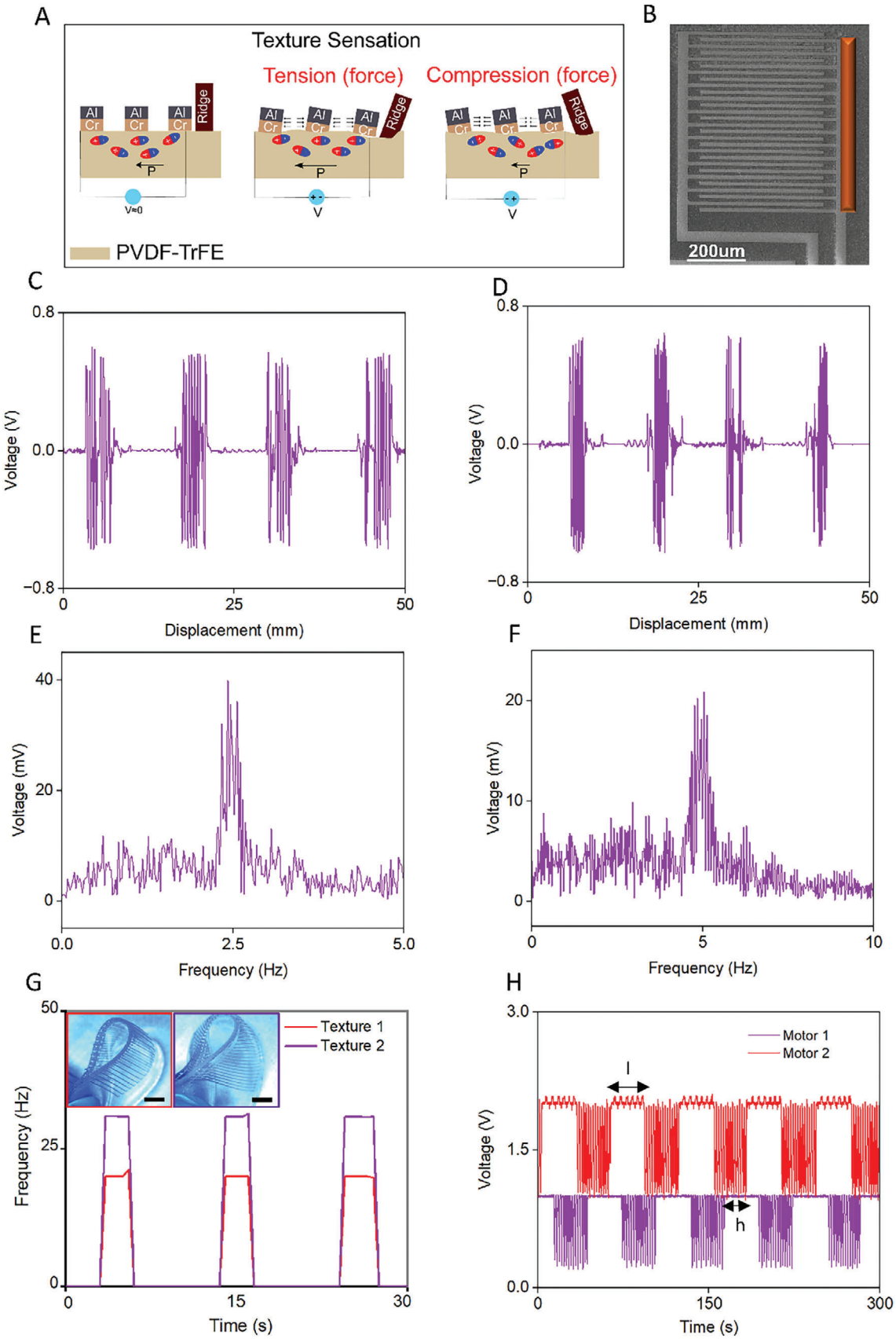

motors corresponds to the roughness of the texture on which the sensor is sliding. In this figure, 'I' represents the off time of the motor and 'h' represents the time delay between the two motors which defines the roughness of the surface.

2.5. In Vivo Trials of the E-Skin System

Validation trials of the e-skin system on human subjects demonstrate the performance and operational robustness of the system under controlled conditions. Tests involve mounting the e-skin system to the upper limb of healthy volunteers ($n = 10$; **Figure** 5A) with varying age groups. The multiplexed array of sensors was initially placed on the middle finger of the participant's hand wearing a glove, but it can also be positioned on any of the fingers on the hand (Koç University Ethics Board Protocol 2017.124.IRB2.038). These locations are important parts of the hand for object manipulation and get sensation when in contact with an object. The participants were wearing a thick glove to isolate the system and prevent the sensations directly on the human skin, and the sensor array was placed on the finger of the glove. The sensor array was connected to the miniaturized electronics by using a flexible cable coming under the glove. Upper limb amputation is an injury in which a person loses their hand below the wrist. To translate the artificial sensation from the prosthetic hands to the healthy part of the human hands, the wrist is to be considered the most sensitive to perceive these sensations. The array of actuators was placed on the wrist of the human by using a hook fastener (Velcro) to hold the actuators and connected to the miniaturized electronics (3×3 cm) through a flexible FFC cable. Next, the participants were guided to wear a face mask and headphones with noise-canceling capabilities while playing white noise to prevent any external sounds from the device or surroundings that could potentially impact the perception of haptics. Since we report four distinct types of sensors, the experiment necessitates four corresponding tests for each sensation. Each experiment was repeated ten times with random patterns of the applied sensations for every participant. An embodiment questionnaire was prepared and presented to the participants to capture their responses qualitatively. At the end of each experiment, participants were asked to complete the questionnaire.

Figure 5B depicts the setup for the temperature sensor experiment. The external temperature is administered to the sensor through a heat gun, while the actuator is positioned on the wrist of the hand. For the texture sensor experiment (Figure 5C), the surface was equipped with a moving stage (LTS150, Thorlabs Inc.) and set to slide at a constant velocity. Participants were instructed to place their hands on a fixed point on the sliding surface. Regarding the feasibility trials for the vibration sensor, the sensor was situated on a beam subject to controlled vibration. Concurrently, the actuator was placed on the wrist of the hand, as shown in Figure 5D. Furthermore, Figure 5E demonstrates the setup for the pressure sensor experiment. The pressure was exerted on the sensor using a force gauge while the actuator remained positioned on the wrist.

Pressure sensation and feedback mechanism are important functions to provide users with a more comprehensive perception of the object. Here, we performed an experiment on the pressure sensor by applying pressure to the sensor, and the actuator was attached to the human wrist. The applied pressure to the sensor with the pattern of the first three soft touches (≈10 kPa) on the sensor followed by two touches and then one touch for a long period. The output of the sensor can be recorded in the form of a change in capacitance when the pressure is applied which different pattern as shown in Figure 5F. The three patterns of pressure were applied to each subject ten times randomly. The change in applied pressure resulted in the change in capacitance which was mapped to the rotation of the arm of the servo motor (pressure actuator) to produce a soft touch sensation on the human skin. The participants were asked to differentiate the applied pattern in the form of a questionnaire based on which statistical analysis was carried out. Overall, the ten participants correctly identified the three different patterns of applied pressure in 96.7% of cases (Figure 5I and for each participant, see Figure S17, Supporting Information). Movie S2 (Supporting Information) demonstrates the real-time trial of the e-skin system for pressure sensation. Based on the confusion matrix, sensitivity, and specificity values were calculated (Figure S18a,b, Supporting Information). The experiment demonstrates that the e-skin system performs well, as evidenced by its high sensitivity score (SE = 0.97) and specificity score (SP = 0.98). This confirms the effectiveness of the e-skin system.

A tactile feedback system of the vibration sensation is realized by integrating the vibration sensor output into the vibration actuator. The vibration sensation from the sensor's output was translated to the ERM vibration actuator via electronic circuitry. The frequency of the waveform was calculated by taking the real-time FFT which gives the dominant frequency. The vibration motor vibrated with the output dominant frequency generated by the sensor. Figure 5I illustrates the vibration pattern applied to the sensor with one vibration at 75 Hz followed by vibrating twice at the same frequency and then three times vibration. The output vibration frequency of the sensor can be seen in Figure 5G which shows the three frequency signals produced in response to the applied vibration patterns. The quantitative results of the experiment were realized in the form of statistical analysis. The confusion matrix illustrates the overall performance of this task with 98% correct answers (Figure 5J, with one subject's output shown in Figure S19, Supporting Information). Moreover, the confusion matrix was utilized to compute sensitivity and specificity values, revealing a notable level of sensitivity (SE = 0.98) and specificity (SP = 0.99) (Figure S20a,b, Supporting Information). The findings demonstrate the system's ability to deliver vibrations to individuals with upper limb amputation at various frequencies.

Figure 4. Performance characteristics of the piezoelectric-based texture sensor and actuator. A) The working mechanism of the piezoelectric-based texture sensor. B) SEM photo of the piezoelectric-based texture sensor. C and E) The output voltage waveform of the texture sensor and its corresponding dominant frequency of 2.5 Hz plot. D and F) The voltage waveform of the texture sensor and FFT results in the dominant frequency of 5 Hz. G) A texture sensor connected to electronics produces two different frequencies when slides on two different texture surfaces for a certain time frame. H) PWM signal of two vibration motors vibrating with a certain delay.

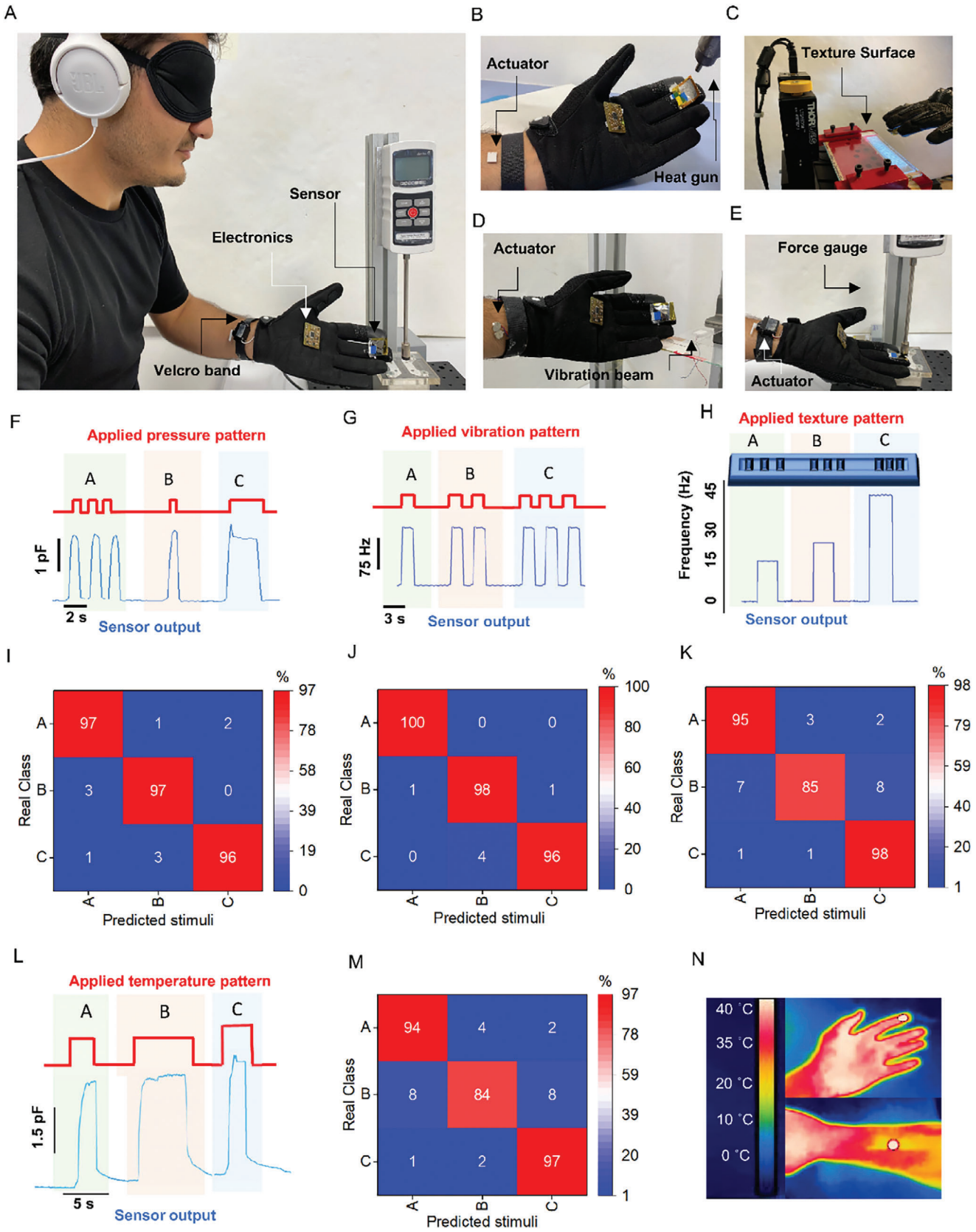

The recognition of tactile textures is an intricate procedure that involves the spatial encoding of the coarse texture's geometric properties and the vibrotactile encoding of the fine textures. We mimicked this mechanism by utilizing a system that integrates the fabricated piezoelectric-based texture sensors with the coin cell ERM vibration motors as a texture actuator. We chose three surfaces of varying roughness: the initial surface featured ridges roughly measuring 1.1 mm with an inter-element spacing of 1.1 mm, the second surface displayed a roughness of the ridge of ≈0.8 mm with inter-element spacing of 0.8 mm, and the third surface exhibited a roughness of ≈0.44 mm with the inter-element spacing of 0.44 mm (Figure S21, Supporting Information). The rough surface was placed on a moving stage with a controlled speed (20 mm s^{-1} in this experiment), and the sensor on the glove was placed on a fixed stage to interact with the moving stage. Figure 5H shows the applied pattern of surfaces having the roughness mentioned above and the sensor's output frequency calculated by taking the real-time FFT in the microcontroller.

Two coin-cell ERM vibration motors were used as an actuators, and the vibration frequency produced by the sensors was given to the motors to vibrate. There was a certain delay between the actuation time of the motors which corresponded to the roughness of the surface. Experimental trials were performed, and participants were asked to differentiate between the three surfaces. Statistical analysis results were shown in the form of a confusion matrix which shows 92.7% accurate answers (Figure 5K; Figure S22, Supporting Information). Furthermore, sensitivity and specificity values of SE = 0.89 and SP = 0.96 are calculated from the confusion matrix (Figure S23a,b, Supporting Information).

The temperature experiment comprises two distinct applied temperature patterns of ≈40 °C and one distinct pattern with a temperature of ≈43 °C to the sensor using a heat gun. Initially, a temperature stimulation for a short duration is administered, succeeded by a substantial stimulation endured for an extended duration. Subsequently, another pattern for a short duration but relatively high-temperature stimulation compared to the two patterns is employed (Figure 5L). The alteration in capacitance, observed as a reaction to the externally applied temperature, represents the sensor's output. The output of the sensor shows a good resemblance to the applied temperature pattern. Thermo-haptic feedback is also a crucial function in providing users with a more comprehensive perception of the object. The temperature actuator responds to the temperature applied to the sensor. A voltage signal is given to the actuator in the form of a pulse when the change in capacitance occurs.

The placement of a temperature actuator on the human wrist and its activation in response to the output of the sensor constitutes the methodology. The participants were asked to differentiate between the applied patterns of temperature and the response was recorded in the form of a questionnaire. The ensuing responses were documented through a questionnaire. Statistical analysis was performed through a confusion matrix, depicted in Figure 5M, displaying a 91.7% accuracy rate. Further calculations of specificity and sensitivity from the matrix revealed sensitivity and specificity values of SE = 0.91 and SP = 0.92, respectively.

To establish a comparison, the actuator was also positioned on the finger and wrist of a participant, enabling discrimination of applied temperatures on distinct body locations. Thermal camera images portray the actuator temperature on both the human wrist and finger, demonstrating uniform temperature (Figure 5N; Figure S24, Supporting Information). The applied temperature can be controlled by the voltage signal to the actuator based on the applied temperature to the sensor. This enables us to differentiate objects with different thermal properties, e.g., differentiating different objects based on their surface thermal state, etc. The real-time trial of the temperature experiment is demonstrated in Movie S3 (Supporting Information).

3. Conclusion

In this study, we introduce a piezoelectric-based e-skin capable of multisensory tactile sensation of the temperature, pressure, vibration, and texture located at the interface between the prosthetic hand and the soft skin of the residual limb. The demonstration of the multifunctional e-skin on different participants without any irritation and thermal or mechanical perturbation of the skin surface illustrates its robust capabilities in the prosthesis. By restoring the sensory feedback mechanism of the prosthesis, this near-natural system significantly enhances the quality of life for individuals with upper limb amputation. Our miniaturized design of the e-skin also contains a sensory feedback system that enables the correct sensory motor integration between the central nervous system of the user and the artificial limb. We tested the real-time implementation of the e-skin system by placing the miniaturized array of sensors on the glove which mimicked an upper limb prosthetic. The real-time feedback mechanism was achieved by using a series of actuators assembled with a miniaturized electronic circuit design attached to the soft skin. The capabilities rely critically on three main advances over the technologies reported previously: i) multifunctional miniaturized design of the e-skin system, ii) miniaturized double-sided design of the integrated electronic circuitry for signal processing

Figure 5. In vivo trial of the e-skin system on human subjects. A) Photograph of the subject performing the experiments, the participant was blindfolded and acoustically shielded. Experimental protocol for B) the temperature sensor while applying temperature by heat-gun; C) the texture sensor by sliding the sensor on a textured surface; D) the vibration sensor by sensing the vibration of known frequency; E) the pressure sensor subjected the sensor to the force gauge. F) Picture of the applied pressure sensor and the output response of the sensor. G) Picture of the applied vibration pattern and the output frequency (75 Hz) response of the sensor. H) Picture of the applied texture surfaces to the sensor and the out frequencies of the sensor. I) The performance was obtained during a control condition where a pressure experiment was performed in the form of a confusion matrix. In every case, 30 repetitions were performed with ten participants. J) Confusion matrix of the response obtained from the vibration experiment. K) Overall performance of the texture sensor and feedback in the form of a confusion matrix. L) Picture of the applied temperature pattern and the output of the temperature sensor. M) The performance obtained during the temperature experiment is in the form of a confusion matrix. N) Thermal images of the actuator applied to the finger and wrist of the human subject.

to make the system standalone and reduce the bulkiness, and iii) the feedback mechanism achieved by using actuators. Compared with the reported e-skins with different working mechanisms, this piezoelectric-capacitive e-skin system is a complete package in terms of the number of comprehensive sensations, linearity, and miniaturized size of an array (Table S1, Supporting Information). Moreover, compared to different e-skins reported, the reported e-skin has some advantages: the miniaturized sensing array possesses four comprehensive sensations with a haptic feedback mechanism, and the sensors exhibit a wide range of sensations which makes the e-skin system to cover the limit of the natural sensation of the human skin (Table S2, Supporting Information). This type of multifunctional tactile sensing system creates a promising route for scalable manufacturing of e-skins, which is highly desired in applications like prosthetics[48,49] and surgeon robots.[50,51]

The miniaturized sensors and electronics strategies hold significant potential, particularly for individuals utilizing wearable robots in rehabilitation. Miniaturizing not just the sensors but also the actuators in designing human-machine interfaces is crucial, as it allows for the overall interface to become more compact. Additionally, this miniaturization enhances the density of stimulation signals, providing more precise and localized feedback for improved interaction. Benchtop studies and practical implementation of the system on an upper limb prosthesis demonstrate the usability of all the critical functional aspects and its adaptability for other types of limb amputations. Future work could focus on establishing wireless connections between the sensors and actuators and integrating an internal power source to eliminate the need for an external power supply. Moreover, optimizing the e-skin system design for other amputations could enhance its versatility.

4. Experimental Section

Fabrication of the Miniaturized Array of Sensor: A standard six-inch silicon wafer (Siegert Wafer Inc.) was diced into 2.5 cm × 2.5 cm small chips using a dicing saw (DAD 3221, DISCO Inc.). These silicon chips served as temporary substrates for the fabrication process. The diced chip was sequentially submerged in acetone and isopropyl alcohol (IPA), each time undergoing a 5-min ultrasonic bath for cleaning. Following, the chip was blow-dried with N2 and treated with oxygen-plasma (SI 500, Sentech Instruments Inc.) for 60 s. Subsequently, the chip was spin-coated with polyimide (PI) (Sigma–Aldrich Inc.) and baked at 100 °C for 1 h, followed by baking at 300 °C for 1 h. Then, aluminum was sputtered to a thickness of 120 nm, followed by the sputtering of 30 nm of chromium onto the aluminum layer (PVD 75 PRO-Line, Kurt J. Lesker Inc.). Subsequently, a solution of 15 wt.%PVDF-TrFE (FC20, Piezotech Inc.) was prepared by mixing PVDF-TrFE powder in dimethylformamide (DMF). The mixture was stirred on a temperature-controlled magnetic stirrer for 3 h at 80 °C and then filtered through a 0.45 µm PTFE membrane. Before applying the PVDF-TrFE layer, Kapton tape was used to cover a small portion of the sputtered metal to ensure a connection with the bottom electrode after fabrication. The PVDF-TrFE solution was first spin coated and baked at 140 °C for 5 min, followed by a second spin coating and baking at the same temperature for 20 min. AZ5214 positive photoresist (AZ5214, MicroChemicals Inc.) was spin-coated and soft-baked at 110 °C for 55 s before patterns were defined with UV photolithography (µMLA 100, Heidelberg Instruments Inc.). AZ 726 MIF developer (AZ 726 MIF, MicroChemicals Inc.) was applied for 110 s for the development. In order to remove excess photoresist from the developed regions, 60 s of oxygen-plasma treatment (SI 500, Sentech Instruments Inc.) was applied. For the top electrode, a 30 nm chromium layer and a 120 nm aluminum layer were sputtered (PVD 75 PRO-Line, Kurt J. Lesker Inc.). Lift-off was performed using methanol to avoid damaging the PVDF-TrFE film. To enhance the piezoelectric properties of the PVDF-TrFE film, polarization was conducted using DC voltage. The voltage gradually increased from 20 V to a final value of 300 V, and the 300 V field was applied for 30 min. See Figure S25 (Supporting Information) for the fabrication flow of the miniaturized array of sensors.

Design of the Miniaturized Circuit: A miniaturized double-sided electronic circuitry was designed for the e-skin system to make the system standalone (Figures S26 and S27, Supporting Information). The circuit included two main sensing mechanisms of the output from the array of sensors. For the static pressure sensor and temperature sensor, the output was observed as a change in capacitance. This change in capacitance was read by the 4-channels CDC IC communicates with the microcontroller via I^2C protocol. The FDC1004 (Texas Instruments, USA) CDChas a full-scale range of ±15 pF, with 0.5 aF resolution a programmable offset capacitance of up to 100 pF, and an active shielding signal output. The CDC has four multiplexed sensing channels and output rates up to 400 Hz. The vibration sensor and texture sensors produce output as a change in voltage which passes through internal ADC in the microcontroller to digitalize the signal at a sampling frequency of 400 Hz. The signal processing unit consists of an surface-mounted device microcontroller (Atmega328p, Microchip Technology Inc.) with a crystal oscillator, resistors, and capacitors as peripheral components. The electronic circuitry communicates with the sensors and actuators through flexible cables. The PCB also contains electronic components for the actuators. The Peltier module was controlled by using an H-bridge (DRV8225, Texas Instruments Inc.) which controls the switches that deliver power to the load. To run the coin cell ERMvibration motor, motor drivers (DRV2605, Texas Instruments Inc.) were used to communicate with the microcontroller through the I^2C protocol. The PCB was connected to a rechargeable lithium-ion (Li-ion) battery (GlobTek Inc.) which powers the whole system.

Statistical Analysis: Four single-blinded experiments focusing on pressure, temperature, vibration, and texture, with ten participants ($n = 10$) were conducted. Each experiment involved the application of three distinct actuation patterns (A, B, C) in a randomized order, repeated three times per pattern. Participants' responses were recorded using a structured questionnaire. Confused matrices were constructed for each actuator and pattern combination to evaluate the performance of the participant's predictions. From the confusion matrix data, it calculated sensitivity (true positive rate) and specificity (true negative rate) values, with sensitivity defined as the proportion of correctly identified positive instances and specificity as the proportion of correctly identified negative instances. All statistical analyses, including the construction of confusion matrices and the calculation of sensitivity and specificity values, were performed using Origin Pro software, which was also used to plot sensitivity and specificity values to visualize performance across different actuators and patterns.

Supporting Information

Supporting Information is available from the Wiley Online Library or from the author.

Acknowledgements

The authors acknowledge the use of the services and facilities of Koç University n2STAR-Koç University Nanofabrication and Nano characterization Center for Scientific and Technological Advanced Research. Also, the authors are thankful to Taher Abbasiasl, Fariborz Mirlou, Rümeysa Emine Cebecioğlu, Pelin Kübra İşgör, Umut Can Yener, and Emine Bardakci for their help during the in vivo studies. LB acknowledges the Scientific and Technological Research Council of Turkey (TUBITAK) as the project received funding from 2232 program (grant no: 118C295). LB acknowledges the Europan Research Council (2ND-CHANCE, grant no: 101043119).

Conflict of Interest

The authors declare no conflict of interest.

Data Availability Statement

The data that support the findings of this study are available from the corresponding author upon reasonable request.

Keywords

capacitance, haptic feedback, multiplexed sensing, piezoelectricity, prosthesis, upper limb amputation

Published online:

[1] K. A. Raichle, M. A. Hanley, I. Molton, N. J. Kadel, K. Campbell, E. Phelps, D. Ehde, D. G. Smith, *J. Rehabil. Res. Dev.* **2008**, *45*, 961.
[2] K. Ziegler-Graham, E. J. MacKenzie, P. L. Ephraim, T. G. Travison, R. Brookmeyer, *Arch. Phys. Med. Rehabil.* **2008**, *89*, 422.
[3] L. A. Jones, S. J. Lederman, *Human Hand Function*, Oxford University Press, Oxford, England **2006**.
[4] J. Yin, R. Hinchet, H. Shea, C. Majidi, *Adv. Funct. Mater.* **2021**, *31*, 2007428.
[5] Y. H. Jung, J.-Y. Yoo, A. Vázquez-Guardado, J.-H. Kim, J.-T. Kim, H. Luan, M. Park, J. Lim, H.-S. Shin, C.-J. Su, *Nat. Electron.* **2022**, *5*, 374.
[6] D. Li, J. He, Z. Song, K. Yao, M. Wu, H. Fu, Y. Liu, Z. Gao, J. Zhou, L. Wei, Z. Zhang, Y. Dai, Z. Xie, X. Yu, *Microsyst. Nanoeng.* **2021**, *7*, 85.
[7] D. Li, J. Zhou, K. Yao, S. Liu, J. He, J. Su, Q. Qu, Y. Gao, Z. Song, C. Yiu, C. Sha, Z. Sun, B. Zhang, J. Li, L. Huang, C. Xu, T. H. Wong, X. Huang, J. Li, R. Ye, L. Wei, Z. Zhang, X. Guo, Y. Dai, Z. Xie, X. Yu, *Sci. Adv.* **2022**, *8*, eade2450.
[8] S. Chen, Y. Chen, J. Yang, T. Han, S. Yao, *npj Flexible Electronics.* **2023**, *7*, 1.
[9] A. Chortos, J. Liu, Z. Bao, *Nat. Mater.* **2016**, *15*, 937.
[10] Z. Liang, J. Cheng, Q. Zhao, X. Zhao, Z. Han, Y. Chen, Y. Ma, X. Feng, *Adv. Mater. Technol.* **2019**, *4*, 1900317.
[11] P. Li, H. P. Anwar Ali, W. Cheng, J. Yang, B. C. K. Tee, *Adv. Mater. Technol.* **2020**, *5*, 1900856.
[12] J. W. Kwak, M. Han, Z. Xie, H. U. Chung, J. Y. Lee, R. Avila, J. Yohay, X. Chen, C. Liang, M. Patel, I. Jung, J. Kim, M. Namkoong, K. Kwon, X. Guo, C. Ogle, D. Grande, D. Ryu, D. H. Kim, S. Madhvapathy, C. Liu, D. S. Yang, Y. Park, R. Caldwell, A. Banks, S. Xu, Y. Huang, S. Fatone, J. A. Rogers, *Sci. Transl. Med.* **2020**, *12*, 4327.
[13] E. D'Anna, G. Valle, A. Mazzoni, I. Strauss, F. Iberite, J. Patton, F. M. Petrini, S. Raspopovic, G. Granata, R. Di Iorio, *Sci. Robot.* **2019**, *4*, eaau8892.
[14] F. M. Petrini, G. Valle, M. Bumbasirevic, F. Barberi, D. Bortolotti, P. Cvancara, A. Hiairrassary, P. Mijovic, A. Ö. Sverrisson, A. Pedrocchi, J. L. Divoux, I. Popovic, K. Lechler, B. Mijovic, D. Guiraud, T. Stieglitz, A. Alexandersson, S. Micera, A. Lesic, S. Raspopovic, *Sci. Transl. Med.* **2019**, *11*, eaav8939.
[15] T. G. Thuruthel, B. Shih, C. Laschi, M. T. Tolley, *Sci. Robot.* **2019**, *4*, 1488.
[16] B. Shih, D. Shah, J. Li, T. G. Thuruthel, Y. L. Park, F. Iida, Z. Bao, R. Kramer-Bottiglio, M. T. Tolley, *Sci. Robot.* **2020**, *5*, 9239.
[17] C. M. Boutry, M. Negre, M. Jorda, O. Vardoulis, A. Chortos, O. Khatib, Z. Bao, *Sci. Robot.* **2018**, *3*, eaau6914.
[18] G. Yao, L. Xu, X. Cheng, Y. Li, X. Huang, W. Guo, S. Liu, Z. L. Wang, H. Wu, *Adv. Funct. Mater.* **2020**, *30*, 1907312.
[19] F. Liu, S. Deswal, A. Christou, M. S. Baghini, R. Chirila, D. Shakthivel, M. Chakraborty, R. Dahiya, *Sci. Robot.* **2022**, *7*, 7286.
[20] Y. Liu, C. Yiu, Z. Song, Y. Huang, K. Yao, T. Wong, J. Zhou, L. Zhao, X. Huang, S. K. Nejad, M. Wu, D. Li, J. He, X. Guo, J. Yu, X. Feng, Z. Xie, X. Yu, *Sci. Adv.* **2022**, *8*, 6700.
[21] Y. Yu, J. Nassar, C. Xu, J. Min, Y. Yang, A. Dai, R. Doshi, A. Huang, Y. Song, R. Gehlhar, A. D. Ames, W. Gao, *Sci. Robot.* **2020**, *5*, eaaz7946.
[22] M. Zhu, Z. Sun, Z. Zhang, Q. Shi, T. He, H. Liu, T. Chen, C. Lee, *Sci. Adv.* **2020**, *6*, eaaz8693.
[23] M. Cai, Z. Jiao, S. Nie, C. Wang, J. Zou, J. Song, *Sci. Adv.* **2021**, *7*, eabl8313.
[24] G. Y. Bae, J. T. Han, G. Lee, S. Lee, S. W. Kim, S. Park, J. Kwon, S. Jung, K. Cho, *Adv. Mater.* **2018**, *30*, 1803388.
[25] Y. Qiu, Y. Tian, S. Sun, J. Hu, Y. Wang, Z. Zhang, A. Liu, H. Cheng, W. Gao, W. Zhang, *Nano Energy.* **2020**, *78*, 105337.
[26] S. Zhao, R. Zhu, *Adv. Mater.* **2017**, *29*, 1606151.
[27] D. Farina, O. Aszmann, *Sci. Transl. Med.* **2014**, *6*, 257ps12.
[28] B. Rostamian, M. Koolani, P. Abdollahzade, M. Lankarany, E. Falotico, M. Amiri, N. V. Thakor, *Sci. Rep.* **2022**, *12*, 21690.
[29] S. J. Bensmaïa, M. Hollins, *Somatosens. Mot. Res.* **2003**, *20*, 33.
[30] Y. Wang, H. Wu, L. Xu, H. Zhang, Y. Yang, Z. L. Wang, *Sci. Adv.* **2020**, *6*, eabb9083.
[31] Y. Chen, H. Lei, Z. Gao, J. Liu, F. Zhang, Z. Wen, X. Sun, *Nano Energy.* **2022**, *98*, 107273.
[32] J. W. Fastier-Wooller, T. Dinh, C.-D. Tran, D. V. Dao, *Mater. Des.* **2021**, *208*, 109886.
[33] Y. Pang, X. Xu, S. Chen, Y. Fang, X. Shi, Y. Deng, Z.-L. Wang, C. Cao, *Nano Energy.* **2022**, *96*, 107137.
[34] G. Lee, J. H. Son, S. Lee, S. W. Kim, D. Kim, N. N. Nguyen, S. G. Lee, K. Cho, *Adv. Sci.* **2021**, *8*, 2002606.
[35] S. Cho, S. Jang, D. Lee, Y. Ra, D. Kam, J. W. Kim, D. Shin, K. D. Seo, D. Choi, *Funct. Comp. Struct.* **2022**, *4*, 045005.
[36] P. Zhu, Y. Wang, Y. Wang, H. Mao, Q. Zhang, Y. Deng, *Adv. Energy Mater.* **2020**, *10*, 2001945.
[37] H. Chen, L. Miao, Z. Su, Y. Song, M. Han, X. Chen, X. Cheng, D. Chen, H. Zhang, *Nano Energy.* **2017**, *40*, 65.
[38] Y. Dai, S. Gao, *IEEE Sens. J.* **2021**, *21*, 26355.
[39] G. Li, S. Liu, Q. Mao, R. Zhu, *Adv. Sci.* **2022**, *9*, 2104969.
[40] W. Xiong, H. Feng, H. Liwang, D. Li, W. Yao, D. Duolikun, Y. Zhou, Y. Huang, *IEEE Sens. J.* **2022**, *22*, 9046.
[41] L. Pan, A. Chortos, G. Yu, Y. Wang, S. Isaacson, R. Allen, Y. Shi, R. Dauskardt, Z. Bao, *Nat. Commun.* **2014**, *5*, 3002.
[42] Y. Zang, F. Zhang, C. Di, D. Zhu, *Mater. Horiz.* **2015**, *2*, 140.
[43] Q. Li, L. Zhang, X. Tao, X. Ding, *Adv. Healthcare Mater.* **2017**, *6*, 1601371.
[44] M. Vicentini, D. Botturi, *Adv. Haptics.* **2010**, 415, https://books.google.com.pk/books?hl=tr&lr=&id=MuqODwAAQBAJ&oi=fnd&pg=PA415&dq=M.+Vicentini,+D.+Botturi,+Advances+in+haptics+2010,+415.&ots=dA9nd6UPbK&sig=MavfQ_84OaoYBRtk6BhYk5cPL84&redir_esc=y#v=onepage&q&f=false.
[45] S. Chun, A. Hong, Y. Choi, C. Ha, W. Park, *Nanoscale.* **2016**, *8*, 9185.
[46] Y. H. Jung, J. Y. Yoo, A. Vázquez-Guardado, J. H. Kim, J. T. Kim, H. Luan, M. Park, J. Lim, H. S. Shin, C. J. Su, R. Schloen, J. Trueb, R. Avila, J. K. Chang, D. S. Yang, Y. Park, H. Ryu, H. J. Yoon, G. Lee, H. Jeong, J. U. Kim, A. Akhtar, J. Cornman, T. il Kim, Y. Huang, J. A. Rogers, *Nat. Electron.* **2022**, *5*, 374.
[47] E. Sotgiu, D. E. Aguiam, C. Calaza, J. Rodrigues, J. Fernandes, B. Pires, E. E. Moreira, F. Alves, H. Fonseca, R. Dias, *J. Microelectromech. Syst.* **2020**, *29*, 629.
[48] J. C. Yang, J. Mun, S. Y. Kwon, S. Park, Z. Bao, S. Park, *Adv. Mater.* **2019**, *31*, 1904765.
[49] H. Zhao, K. O'brien, S. Li, R. F. Shepherd, *Sci Robot.* **2016**, *1*, eaai7529.
[50] D. Wei, J. Guo, Y. Qiu, S. Liu, J. Mao, Y. Liu, Z. Chen, H. Wu, Z. Yin, *Natl. Sci. Rev.* **2022**, *9*, nwac227.
[51] J. Zhu, L. Lyu, Y. Xu, H. Liang, X. Zhang, H. Ding, Z. Wu, *Adv. Intell. Syst.* **2021**, *3*, 2100011.